

Nonrigid Registration of Dynamic Breast F-18-FDG PET/CT Images Using Deformable FEM Model and CT Image Warping

Alphonso Magri¹, Andrzej Krol^{2,1,4M}, Mehmet Unlu⁴, Edward Lipson^{1,2,4}, James Mandel³, Wendy McGraw⁵, Wei Lee¹, and Ioana Coman^{2,4,6} and David Feiglin²

¹Department of Physics, Syracuse University, Syracuse, NY 13244

²Department of Radiology, SUNY Upstate Medical University, Syracuse, NY 13210

³Department of Civil and Environmental Engineering, Syracuse University, Syracuse, NY 13244

⁴Department of Electrical Engineering and Computer Science, Syracuse University, Syracuse, NY 13244

⁵CNY PET, LLP, 5100 W Taft Road, Suite 1A, Liverpool, NY 13088

⁶Department of Mathematics and Computer Science, Ithaca College, Ithaca, NY 14850

ABSTRACT

This study was undertaken to correct for motion artifacts in dynamic breast F-18-FDG PET/CT images, to improve differential-image quality, and to increase accuracy of time-activity curves. Dynamic PET studies, with patients prone, and breast suspended freely employed a protocol with 50 frames, each 1-minute long. A 30 s long CT scan was acquired immediately before the first PET frame. F-18-FDG was administered during the first PET time frame. Fiducial skin markers (FSMs) each containing ~ 0.5 μCi of Ge-68 were taped to each breast. In our PET/PET registration method we utilized CT data. For corresponding FSMs visible on the 1^{st} and n^{th} frames, the geometrical centroids of FSMs were found and their displacement vectors were estimated and used to deform the finite element method (FEM) mesh of the CT image (registered with 1^{st} PET frame) to match the consecutive dynamic PET time frames. Each mesh was then deformed to match the 1^{st} PET frame using known FSM displacement vectors as FEM loads, and the warped PET time-frame volume was created. All PET time frames were thus nonrigidly registered with the first frame. An analogy between orthogonal components of the displacement field and the temperature distribution in steady-state heat transfer in solids is used, via standard heat-conduction FEM software with “conductivity” of surface elements set arbitrarily significantly higher than that of volume elements. Consequently, the surface reaches steady state before the volume. This prevents creation of concentrated FEM loads at the locations of FSMs and reaching incorrect FEM solution. We observe improved similarity between the 1^{st} and n^{th} frames. The contrast and the spatial definition of metabolically hyperactive regions are superior in the registered 3D images compared to unregistered 3D images. Additional work is needed to eliminate small image artifacts due to FSMs.

Keywords : nonrigid 3D image registration, dynamic breast PET/CT, differential images, deformable FEM soft tissue model

1. Introduction

Breast cancer is one of the most common cancers among women in the U.S.^{1,2}. False-positive mammographic screens²⁰, equivocal and/or difficult-to-interpret ultrasound and clinical exams are still a notable fraction of all exams. The preferred method of breast cancer diagnosis is breast biopsy. However, it is relatively expensive (average billed charges are \$3,400^{6,10}), highly invasive and possibly painful procedure that might result in complications such as pneumothorax (3%), hematomas (7%), infection, ecchymosis, and pain (in 33% -69% of patients). In addition, it produces scar tissue that might complicate future mammographic examinations. Approximately 50% of biopsies are negative²⁷. This translates to over 300,000 of retrospectively unnecessary biopsies every year in the US⁶. There is a great need to lower this number. The image data provided by the state-of-the-art F-18-FDG PET/CT dynamic breast scans^{8,13,21,24,28} might result in improved diagnostic accuracy and confidence of radiologists performing exam, as well as in faster diagnosis,

^M corresponding author, email: krola@upstate.edu, phone: 315-464-7054

and would be a useful adjunct to conventional x-ray mammography and ultrasonography for ambiguous cases. In this paper we investigate the new approaches to increase specificity and sensitivity of F-18-FDG PET/CT dynamic breast scans via improvement of the differential images quality through nonrigid image registration in 3D.

2. Materials and Methods

Dynamic PET studies, with patient prone and breasts freely suspended, were performed immediately after intravenous administration of 10 mCi F-18-FDG using a 50-frame protocol ($N=50$ frames of 1 minute each). A dedicated PET/CT system was used (GE Discovery ST scanner and 4-slice CT). The F-18-FDG (administered during first PET time frame acquisition) was injected in the medial antecubital vein (22 or 20 gauge needle) in the contra lateral side to the breast with suspicious lesion. A CT scan with attenuation correction (1 bed position, 40 seconds, 140 kVp, 120 mA, helical scan) was acquired immediately before the first time frame. PET dynamic acquisition was performed with 2D with septa, 50 scans at 1 minute each, for a total of 50 minutes. PET reconstruction was accomplished with 4.25 mm voxel size, in 128x128 matrix, 47 slices per bed position, diameter 60 cm, OSEM algorithm, 30 subsets, 2 iterations, post filter: 6.0 mm, loop filter: 4.7 mm, with Z-axis filter, measured CT attenuation correction, randoms corrected by singles, with correction for deadtime, correction for decay, correction for geometry, scatter compensation by fitting, well counter corrected for sensitivity and activity.

Up to nine fiducial skin markers (FSMs), each containing 0.5 μ Ci of Ge-68, were taped to each breast. Since boundaries of PET volumes are poorly defined, we implemented an indirect approach to nonrigid dynamic breast F-18-FDG PET/CT image registration. The target image is the first dynamic PET time frame, while the floating images are the remaining consecutive dynamic scans. In the first phase, corresponding FSMs visible on the 1^{st} and n^{th} time frame are identified and their geometrical centroids are found, using a knowledge-based semi-automated algorithm, allowing estimation of FSM displacement vectors. Next, an FEM mesh is obtained for the CT breast image, followed by application of FEM to estimate deformation of the CT volume required to conform with displacement vectors observed in consecutive PET time frames. Thus, $N-1$ deformed CT volumes and their FEM meshes are created, each corresponding to $N-1$ consecutive dynamic PET time frames, where N is the total number of time frames. Therefore, all PET time-frame volumes are properly meshed. Next, each PET time-frame mesh is deformed using known FSM displacement vectors as FEM loads. This step is followed by creation of the warped PET time-frame volume. As a result, all PET time frames are nonrigidly registered with the first time frame. A flow chart of this method can be found in Fig.1. In our FEM model, a dense displacement field is obtained by first distributing the Cartesian components of the observed FSM displacement vectors linearly over the breast surface, and then by distributing them throughout the breast volume. An analogy between orthogonal components of the displacement field and the temperature field in steady-state heat transfer (SSHT) in solids is used, via standard heat-conduction FEM software with “conductivity” of surface elements set arbitrarily significantly higher (here by a factor of 1,000) than that of volume elements. Because the surface “conductivity” is set significantly higher than the bulk “conductivity” the surface reaches steady state before the volume. This prevents creation of concentrated FEM loads at the locations of FSMs. Such point load would lead to a wrong FEM solution with large displacements at the FSMs locations and very small displacements elsewhere. A commercial FEM package (ANSYS¹) is used for meshing and FEM calculations. The floating image is warped to a fixed image using an appropriate shape function⁷ for interpolation from mesh nodes to voxels.

3. Results

We observe systematic increase in similarity for all the time frames in the nonrigidly registered images, as compared to non-registered frames. The results of the similarity measurements for three subjects are collected in Table 1. Two large volumes of interest, one for each breast volume, were used for each subject. Figure 2 shows examples of Normalized Mutual Information (NMI), Normalized Correlation Coefficient (NCC), and the Sum of Absolute Valued Differences (SAVD) calculated between the n^{th} and the 1^{st} time frame for the registered and the unregistered images. We have investigated the total integrated activity (corrected for the physical decay) within breast tissue and observed that it steadily declined with time for all subjects. It could be explained by cumulative washout process of F-18-FDG from the breast tissue. Such washout process could explain trends seen in all the graphs in Fig. 2. Differential dynamic PET breast images were obtained for several subjects (examples are shown in Figs. 3 and 4). We observe that contrast and spatial

¹ Info about ANSYS

definition of the suspicious lesions are superior in the registered differential images (Figs. 3 and 4, right column), as compared to the unregistered images (Fig. 3 and 4, left column). The small dark regions seen on the registered images are artifacts due to FSMs. Figure 5 presents Time Activity Curves (TACs) that have been corrected for radioactive decay of the F-18. We observe that the TACs of the metabolically active regions in the registered images reach larger SUV values than in the unregistered images. The normal tissue shows little difference between registered and unregistered data. These findings are collected in Table 2.

4. Conclusions

The method for nonrigid registration of dynamic PET breast time series presented here has yielded significantly improved quality of differential dynamic PET breast images and time activity curves. In some cases, it has revealed metabolically active lesions, difficult to observe in unregistered images. The trends found in all similarity plots vs. time are due to the steady washout of F-18FDG from the breast tissue. More work is needed to eliminate small image artifacts due to fiducial skin markers.

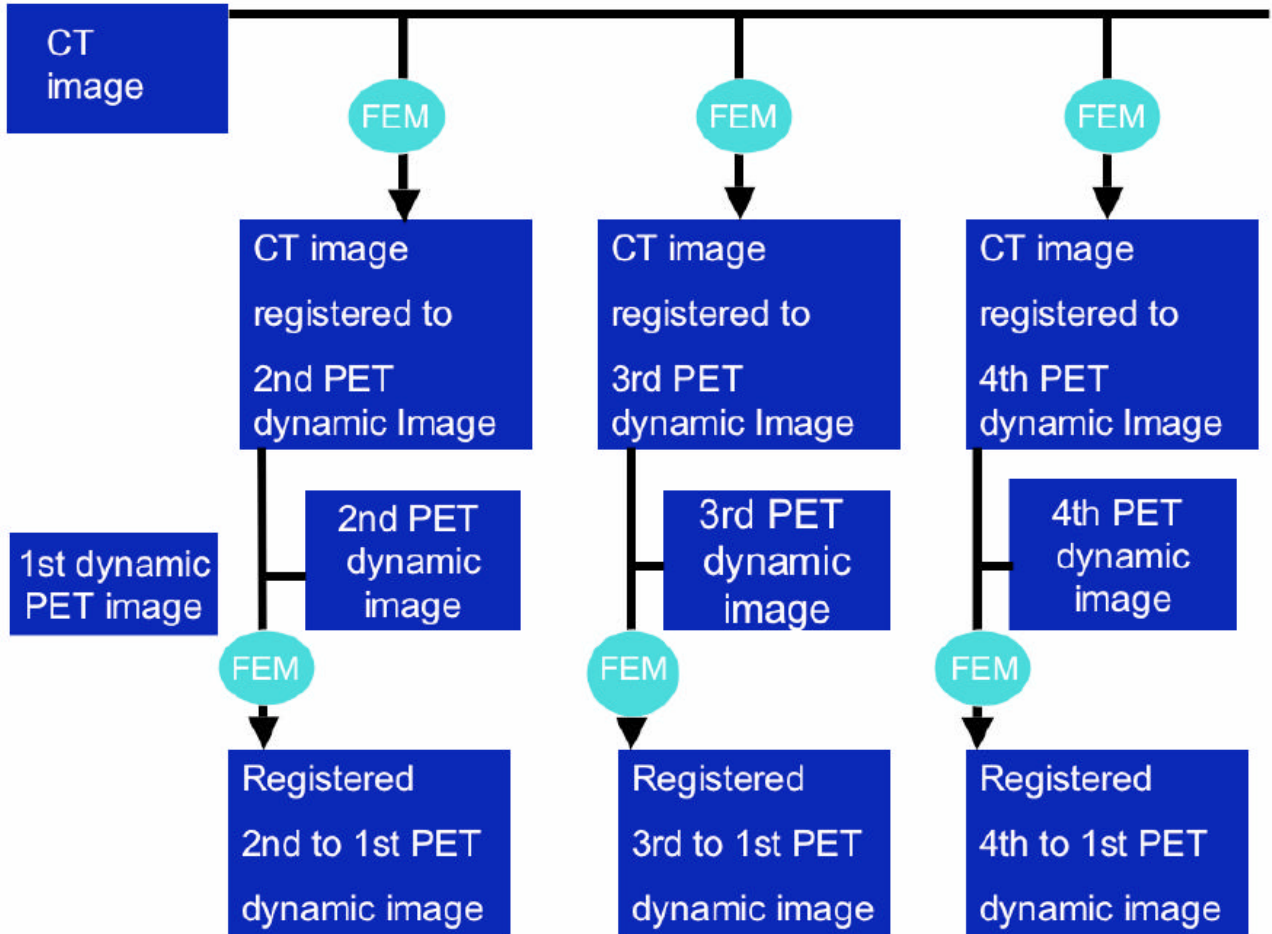


Fig. 1. Flowchart for PET-PET registration.

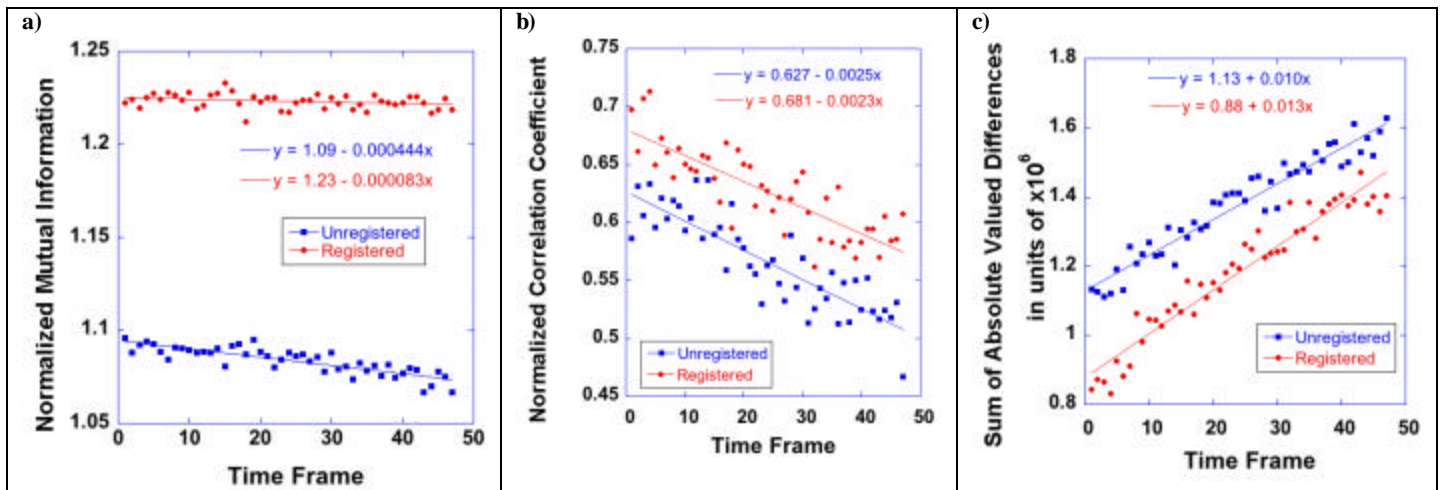


Fig. 2. (a) Normalized Mutual Information (NMI), its range is from 0 to a maximum value of 2. (b) Normalized Correlation Coefficient (NCC), its range is from -1 to a maximum value of 1. (c) Sum of Absolute Valued Differences between n^{th} and 1^{st} time frames for registered and unregistered images. Red circles: registered data. Blue squares: unregistered data.

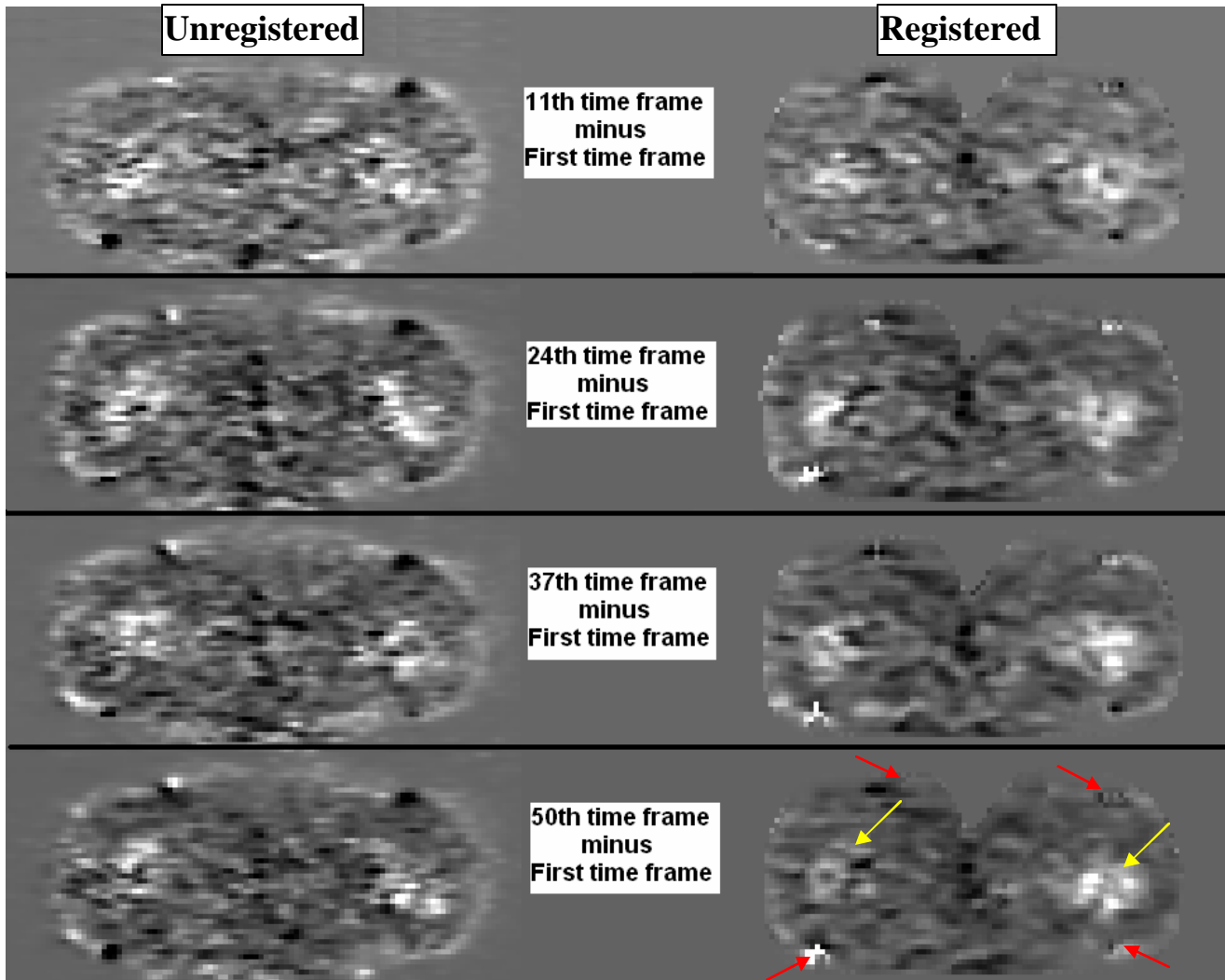


Fig. 3. Coronal views of the differential dynamic F-18-FDG PET images. Left column: differential images obtained by direct subtraction of the first time frame from consecutive unregistered time frames. Right column: nonrigidly registered differential images. Yellow arrows: suspicious metabolically active regions that do not appear as well defined in the unregistered images. Red arrows: FSM artifact.

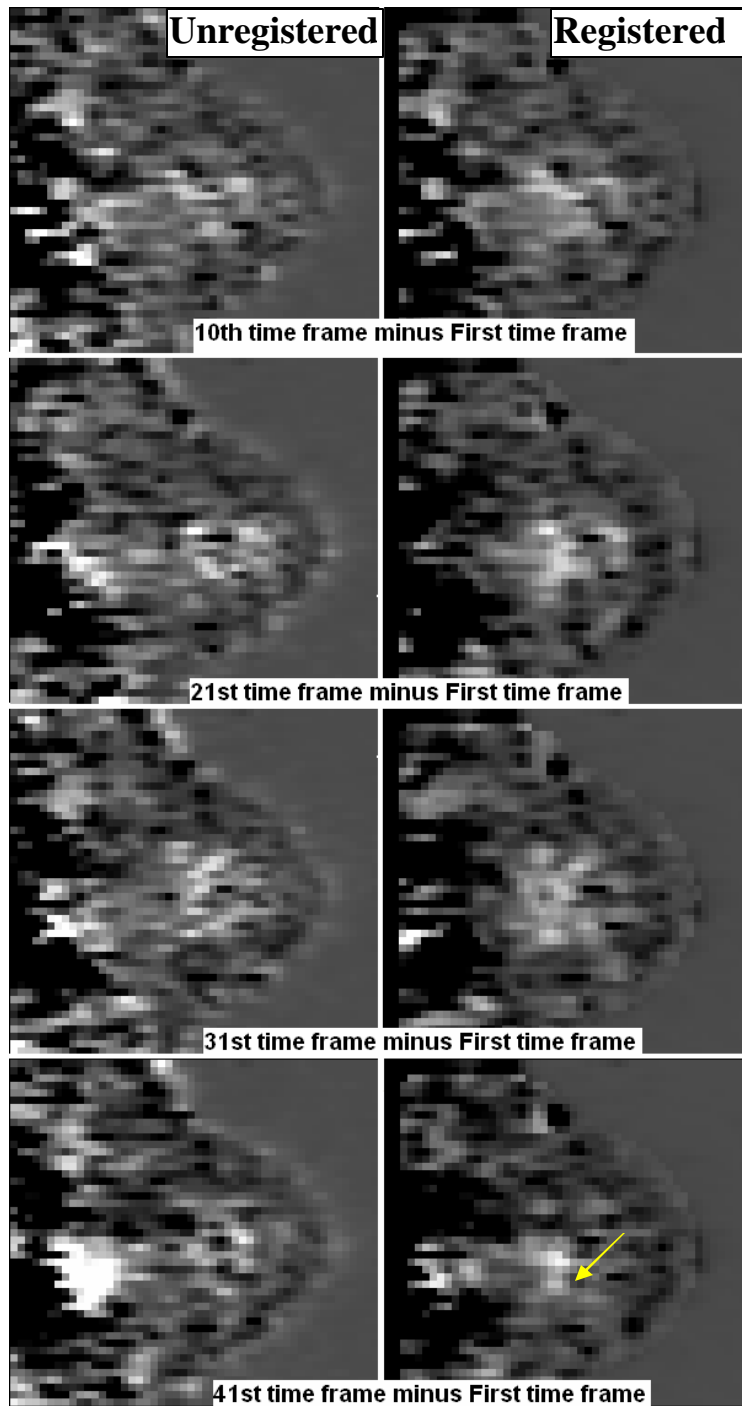


Fig. 4. Sagittal views of the differential dynamic F-18-FDG PET images. Left column: differential images obtained by direct subtraction of the initial time frame from unregistered time frames. Right column: nonrigidly registered differential images. Yellow arrow: suspicious metabolically active regions that do not appear as well defined in the unregistered data.

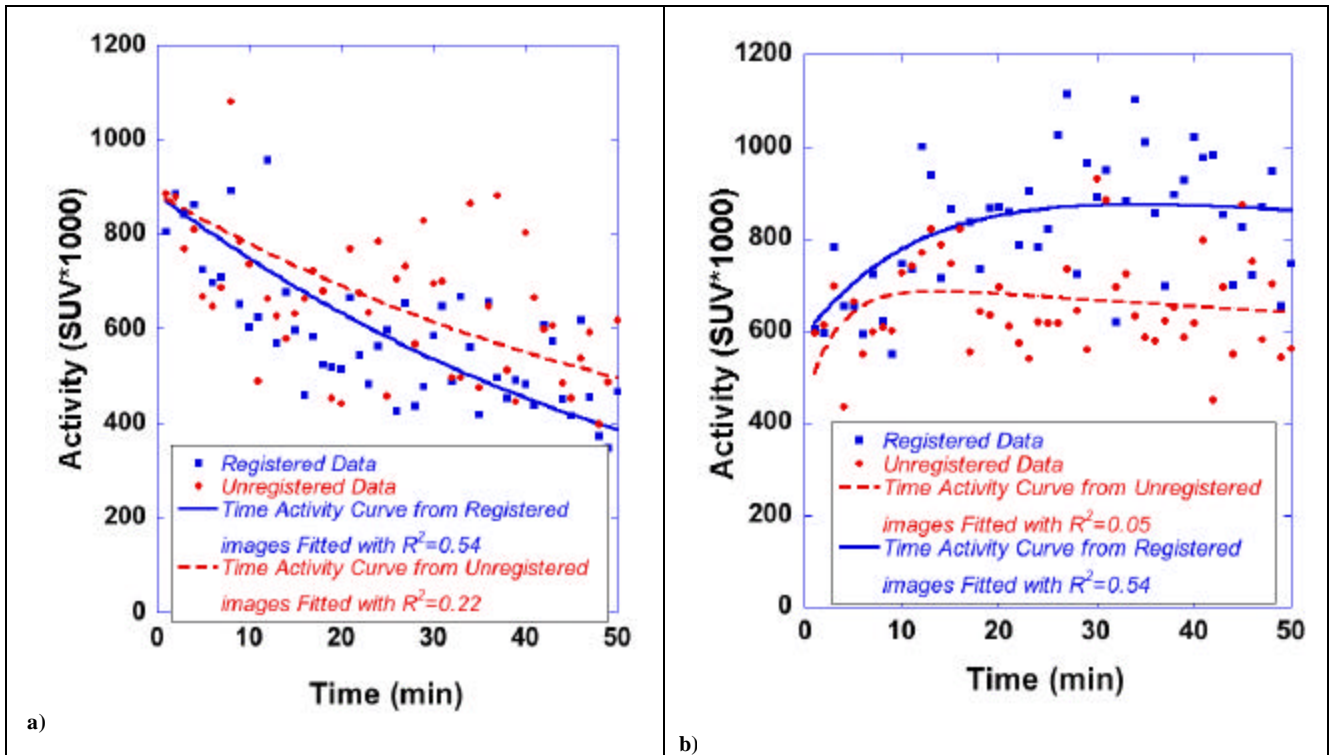


Fig. 5. Time-activity curves for two regions of interest. (a) Metabolically active region; (b) Normal region. Time-activity curves (TAC) have been corrected for natural decay. Red solid circles: data from unregistered images. Blue solid squares: data from registered images. Red dashed line: TAC for unregistered images fitted to a two compartment mathematical model¹⁹. Blue solid line: TAC for registered images fitted to a two compartment mathematical model¹⁹.

Table. 1a. The results of the similarity measurements for large Volumes of Interest (VOI) for 3 subjects. VOI 1 and VOI 2 were defined in the left and right breast, respectively.

Similarity measurements	Subject 46, VOI 1		Subject 46, VOI 2		Subject 47, VOI 1	
	Unprocessed	Processed	Unprocessed	Processed	Unprocessed	Processed
Minimum NMI	1.066	1.212	1.042	1.173	1.039	1.128
Average NMI	1.084	1.223	1.052	1.182	1.059	1.152
Maximum NMI	1.096	1.233	1.060	1.187	1.093	1.168
% Difference in NMI between registered and unregistered images	12.8 %		12.4 %		8.7 %	
Standard deviation, in parenthesis it is given as % of average NMI	0.007 (0.67 %)	0.004 (0.36 %)	0.005 (0.44 %)	0.004 (0.34 %)	0.015 (1.38 %)	0.009 (0.83 %)
Average NCC	0.566	0.627	0.724	0.795	0.619	0.723
% Difference in NCC between registered and unregistered images	10.6 %		9.8 %		16.8 %	
Average SAVD	1.378×10^6	1.159×10^6	0.863×10^6	0.751×10^6	1.455×10^6	1.123×10^6
% Difference in SAVD between registered and unregistered images	15.9 %		13.0 %		22.8 %	

NMI= Normalized Mutual Information, NCC =normalized correlation coefficient, SAVD = the Sum of Absolutely Valued Differences

Table 1.b. The results of the similarity measurements for large Volumes of Interest (VOI) for 3 subjects. VOI 1 and VOI 2 were defined in the left and right breast, respectively.

Similarity measurements	Subject 47, VOI 2		Subject 48, VOI 1		Subject 48, VOI 2	
	Unprocessed	Processed	Unprocessed	Processed	Unprocessed	Processed
Minimum NMI	1.079	1.242	1.035	1.145	1.045	1.132
Average NMI	1.114	1.259	1.066	1.172	1.071	1.144
Maximum NMI	1.147	1.273	1.114	1.195	1.116	1.161
% Difference in NMI between registered and unregistered images	13.0 %		9.9 %		6.8 %	
Standard Deviation, in parenthesis it is given as % of average NMI	0.017 (1.55 %)	0.006 (0.57 %)	0.024 (2.25 %)	0.010 (0.98 %)	0.022 (2.07 %)	0.007 (0.62 %)
Average NCC	0.823	0.847	0.654	0.729	0.760	0.797
% Difference in NCC between registered and unregistered images	2.9 %		11.5 %		4.9 %	
Average SAVD	0.888×10^6	0.752×10^6	2.187×10^6	1.789×10^6	2.467×10^6	1.984×10^6
% Difference in SAVD between registered and unregistered images	15.3 %		18.2 %		19.6 %	

Table 2. Parameters of time-activity curves shown in Fig. 5.

Parameters of time activity curves	Metabolically active region		Normal tissue region	
	Registered Images	Unregistered Images	Registered Images	Unregistered Images
Maximum SUV intensity	1.922	1.072	0.552	0.509
Integrated SUV intensity	61.478	40.427	18.584	18.020

5. ACKNOWLEDGEMENTS

This work was supported in part by Carol M. Baldwin Breast Cancer Research Award.

6. REFERENCES

1. C. C. Boring, T. S. Squires, T. Tong, and S. Montgomery, "Cancer statistics, 1994," *Cancer Journal for Clinicians* 44(1), 7-26, (1994).
2. American Cancer Society, What Are the Key Statistics for Breast Cancer? , <http://www.cancer.org>, 2004.
3. A. Krol, M. Z. Unlu, K. G. Baum, J. A. Mandel, W. Lee, I. L. Coman, E. D. Lipson, and D. H. Feiglin, "MRI/PET nonrigid breast-image registration using skin fiducial markers," *Physica Medica*, (2005). [in print]
4. M. Z. Unlu, A. Krol, I. L. Coman, J. A. Mandel, K. G. Baum, W. Lee, E. D. Lipson, and D. H. Feiglin, "Deformable Model for 3D Intramodal Nonrigid Breast Image Registration with Fiducial Skin Markers," *Proceedings of SPIE*, 5747, 1528-1534 (2005).
5. K. G. Baum, M. Helguera, and A. Krol, "A New Application for Displaying and Fusing Multimodal Data Sets," *CBIOS Proceedings*, (2007).
6. M. Bloomstone, P. D'Angelo, D. Galliano et al., "One Hundred Consecutive Advanced Breast Biopsy," *Annals Sur. Onc.* 6 , 195-199 (1999).
7. O. C. Zienkiewicz and R. L. Taylor, *The Finite Element Method*, McGraw Hill Book Co. New York, 1987.
8. E. Bombardieri and F. Crippa, "PET imaging in breast cancer," *Quat, J. Nuc. Med.* 45, 245-256 (2001).
9. J. R. Buscombe and I. Khalkhali, "Scintimammography with Single-Photon Tracers. *Nuclear Oncology Diagnostic and Therapy, I*," Philadelphia, 273-287, 2001.
10. J. H. Burkhardt and J. H. Sunshine, "Core-Needle and Surgical Breast Biopsy: Comparison of Three Methods of Assessing Cost," *Radiology*, 212, 181-188.
11. P. A. Eliat, V. Dedieu, et al., "Magnetic resonance imaging contrast-enhanced relaxometry of breast tumors: an MRI multicenter investigation concerning 100 patients," *Magnetic resonance imaging* 22, 475-81 (2004) .
12. P. Gibbs, G. P. Liney, et al., "Differentiation of benign and malignant sub-1 cm breast lesions using dynamic contrast enhanced MRI," *Breast* 13, 115-21 (2004).
13. S. I. Heiba, S. Bernik, B. Raphael, N. Sandella, W. Cholewinski, and P. Klein. "The distinctive role of positron emission tomography/computed tomography in breast carcinoma with brown adipose tissue 2-fluoro-2-deoxy-d-glucose uptake," *Breast J.* 11(6), 457-61 (2005).
14. A. Krol, I. L. Coman, J. Mandel, M. Luo, D. H. Feiglin, E. D. Lipson, and J. Beaumont, "Inter-modality nonrigid breast image registration using Finite-Element Method," *IEEE Nuclear Science Symposium and Medical Imaging Conference Record* (2003).
15. A. Krol, M. Z. Unlu, K. G. Baum, J. A. Mandel, W Lee, I. L. Coman, E. D. Lipson, and D. H. Feiglin, "MRI/PET nonrigid breast-image registration using skin fiducial markers," *Physica Medica*, (2006) -in print.

16. A. Krol, A. Magri, M. Unlu, D. Feiglin, E. Lipson, J. Mandel, G. Tillapaugh-Fay, W. Lee, and I. Coman, "Motion Correction via Nonrigid Coregistration of Dynamic MR Mammography Series," *Proceedings of SPIE*, 6142, (2006a).
17. A. Krol, A. Magri, M. Unlu, D. H. Feiglin, E. D. Lipson, J. Mandel, W. Lee, and W. McGraw, "Improved dynamic F-18-FDG PET/CT breast cancer imaging," *World J. Nuc. Med.* (2006b) – in print.
18. T. Makela, P. Clarysse, O. Sipila, et al., "A Review of Cardiac Image Registration Methods," *IEEE TMI* 21, 1011-1021 (2002).
19. E. Laffon, M. Allard, R. Marthan, and D. Ducassou, "A method to quantify the uptake rate of 2-[18F]fluoro-2-deoxy-D-glucose in tissues," *Nuc. Med. Comms.* 25(8), 851–854 (2004).
20. A. Mendez, F. Cabanillas, et al., "Evaluation of Breast Imaging Reporting and Data System Category 3 mammograms and the use of stereotactic vacuum-assisted breast biopsy in a nonacademic community practice," *Cancer* 100, 710-4 (2004).
21. T. H. Palmedo, J. Hensel, M. Reinhardt, D. Von Mallek, A. Matthies, and H-J. Biersack, "Breast cancer imaging with PET and SPECT agents: an in vivo comparison," *Nuclear Medicine and Biology* 29, 809–815 (2002).
22. L. Preda, G. Villa, S. Rizzo, L. Bazzi, D. Origi, E. Cassano, and M. Bellomi, "Magnetic resonance mammography in the evaluation of recurrence at the prior lumpectomy site after conservative surgery and radiotherapy," *Breast Cancer Res.* 8(5),R53 (2006). [Epub ahead of print]
23. S. L. Sailer, J.G. Rosenman, M. Soltys, T. J. Cullip, and J. Chen, "Improving treatment planning accuracy through multimodality imaging," *Int. J. Radiation Oncology* 35, 117-124 (1996).
24. K. Scheidhauer, C. Walter and M. D. Seemann, "FDG PET and other imaging modalities in the primary diagnosis of suspicious breast lesions," *Eur J Nucl Med Mol Imaging* 31(Suppl. 1), S70–S79 (2004).
25. E. J. Somer, P. K. Marsden, et al. "PET-MR image fusion in soft tissue sarcoma: accuracy, reliability and practicality of interactive point-based and automated mutual information techniques," *European Journal of Nuclear Medicine and Molecular Imaging* 30, 54-62 (2003).
26. T. W. Vomweg, A. Teifke, et al., "Combination of low and high resolution sequences in two orientations for dynamic contrast-enhanced MRI of the breast: more than a compromise," *European Radiology*, (2004).
27. C. J. Baines, "Menstrual cycle variation in mammographic breast density: so who cares?," *J. Natl. Cancer Inst.* 90(12), 875-6 (1998).
28. R. L. Wahl, "Current status of PET in breast cancer imaging, staging, and therapy," *Semin Roentgenol* 36(3), 250-60 (2001).